



The effect of MgO on the biodegradation, physical properties and biocompatibility of a Mg/HA/MgO nanocomposite manufactured by powder metallurgy method



Shahrouz Zamani Khalajabadi ^a, Mohammed Rafiq Abdul Kadir ^{a, *}, Sudin Izman ^b, Mohsen Marvibaigi ^a

^a Medical Devices & Technology Group (MEDITEG), Faculty of Biosciences and Medical Engineering, Universiti Teknologi Malaysia (UTM), 81310, Johor Bahru, Johor, Malaysia

^b Department of Materials, Manufacturing and Industrial Engineering, Faculty of Mechanical Engineering, Universiti Teknologi Malaysia (UTM), 81310, Johor Bahru, Johor, Malaysia

ARTICLE INFO

Article history:

Received 2 July 2015

Received in revised form

6 September 2015

Accepted 13 September 2015

Available online 25 September 2015

Keywords:

Mg/HA/MgO

Biocorrosion

Nanorods

Contact area

Corrosion products

Cell culture

ABSTRACT

Recently, magnesium-hydroxyapatite composites have shown the potential to serve as biodegradable metal matrix composite implants that can repair load-bearing defects in osseous tissue. However, the mechanical properties and corrosion resistance of magnesium-hydroxyapatite composites have been restricted by the significant agglomeration of HA particulates. In this study, the bio-corrosion properties of a Mg/HA-based composite were improved by the addition of different amounts of hydroxyapatite (HA) and periclase (MgO) nanopowders to pure magnesium and fabrication of the Mg/HA/MgO nanocomposites using a blend-cold press-sinter powder metallurgy (PM) technique. X-ray diffraction, X-ray photoelectron spectroscopy, transmission electron microscopy, atomic force microscopy and field-emission scanning electron microscopy were used to characterize the compositions of the corrosion products and the surface morphologies of the corroded specimens. Based on the electrochemical test, the corrosion resistance of the nanocomposites is shown to increase from 0.25 kΩ cm² to 1.23 kΩ cm² with the addition of 10 wt% MgO; however, the ultimate compressive strength decreased from ~237 to ~198 MPa. During immersion test in SBF solution, the growth of the Mg(OH)₂ nanorods on the Mg-12.5HA-10MgO and Mg-5HA-15MgO (wt%) nanocomposites increased the contact angle between the SBF solution and the substrate; as a result, the corrosion rate decreased compared to that of the Mg-27.5HA-10MgO and Mg-20HA-5MgO (wt%) nanocomposites. The corrosion products formed on the nanocomposites surface are shown to be primarily Mg(OH)₂, HA, Ca₃(PO₄)₂ and amorphous CaP compounds. The cell culture results indicated that the Mg/HA/MgO nanocomposites remained biocompatible with osteoblasts by increasing of MgO amount.

© 2015 Elsevier B.V. All rights reserved.

1. Introduction

In vivo application of the typical biomedical metals and alloys include austenitic stainless steel (SS), Co–Cr alloys, pure Ti and its alloys, Ni-based and Ta-based alloys, which fabricated into plates, screws and pins to repair serious bone fractures or to assist in the healing process, require removal after healing of tissue by second surgical operation [1–4]. The need for additional surgery increases

the patient suffering with extra surgical cost. In contrast, no additional surgery is required to remove biodegradable materials because these implants dissolve in physiological environment after the healing process is completed [5]. Magnesium and its corrosion products have excellent biocompatibility, and thus Mg has garnered significant attention as a biomaterial for temporary medical implants [6–8]. The mechanical and physical properties of natural bone are found quite similar to pure magnesium but are different with those of the conventional metallic implants that may leads to generation of stress and instability of implants [9]. Initially excellent biocompatibility causes Mg based materials are first introduced as metallic biodegradable implant material but high

* Corresponding author.

E-mail addresses: shahroozamany@yahoo.com (S.Z. Khalajabadi), rafiq@biomedical.utm.my (M.R. Abdul Kadir).

corrosion rate of Mg alloys leads to application of more corrosion resistance materials such as stainless steel, Ti, etc. Localized corrosion was also observed during in vitro and in vivo tests of Mg based alloys such as AZ91, AZ31, WE43 and LAE442 [6,10–12].

Furthermore, Mg corrosion process involves the evolution of hydrogen gas, which accumulates in vivo adjacent to the implant. The H₂ gas and subsequent formation of hydrogen bubbles can noticeably impair other clinical applications of Mg. Alkalization of the surrounding tissues due to the H₂ gas is another drawback of using Mg in these types of applications [13–15]. Thus, it is essential to increase the corrosion resistance of Mg and its alloys to meet the requirements of both implant biodegradation and new bone formation [16,17]. The fabrication of Mg-based metal matrix composites (MMCs) reinforced by bioceramics of natural human bone compositions, such as hydroxyapatite (HA) [18–22] and β -tricalcium phosphate (β -TCP) [23–25], are currently being studied as promising biomaterials based on their higher specific stiffness and strength as well as their minimal sensitivity to galvanic corrosion. The HA has unique feature of biocompatibility than other phosphate groups. The HA particles show very low solubility as compared to β -TCP in our body fluid [3,26,27]. However, poor load bearing capability of HA results in limited applications [27]. The combination of pure magnesium and HA would be a promising approach to fabricate a metal matrix composite (MMC) as biomaterial with optimum properties. Several metal matrix composites such as Ti–HA, Ti–6Al–4V–HA, AZ91–HA, etc. have been developed to obtain the required properties [18,28,29]. From a biocompatibility point of view, the Mg based matrix would be better than Ti matrix.

Mg/HA composites have been developed via melting and extrusion by Khanra et al. [30]. The dispersion of different amounts of HA powder (0, 5, 10, and 15 wt%) into melted magnesium was performed by mechanical stirring. 15 wt% of HA particles in a Mg/HA composite increased the compressive yield strength of the Mg/HA composite from ~65.8 to ~147.15 MPa [30]. However, the differences in the melting points of Mg and the bioceramic additives (e.g., HA, β -TCP, Ca₂(PO₄)₃, MgO, TiO₂, and ZrO₂) and the complex atmospheric control required during casting created defects in the as-cast samples; these difficulties have led to the powder metallurgy methods having more potential to fabricate Mg/bioceramic composites. Witte et al. [18] prepared the AZ91D/HA (20 wt%) metal matrix composite via the powder metallurgy method and found it to be cytocompatible biomaterial with improved corrosion resistance compared to that of bulk AZ91D alloy. The powder metallurgy method was used to prepare the Mg/HA (10, 20 and 30 wt%) composites with pure magnesium and hydroxyapatite powders. An increase was observed in the yield tensile strength of Mg/10wt% HA composite compared to that of the as-extruded bulk pure magnesium; however, a further increase in the HA content decreased the yield strength, ultimate tensile strength and elongation of the Mg/HA composites. With regard to the cytotoxicity tests, no significant toxicity to L-929 cells was observed for the Mg/20 wt% HA composite [19].

However, HA alone has some disadvantages, such as (i) the low melting point of phosphorus, (ii) the low bonding strength of HA to the metal substrate, and (iii) the agglomeration of HA particles during fabrication, which will ultimately lead to loosening and failure of the Mg-based composites [30,31]. To overcome these problems, bioactive ceramics such as TiO₂, ZrO₂ and MgO powders, which exhibit higher chemical stabilities compared with that of the apatite structure, were added to the matrix of the composite to improve the bioactivity, biocorrosion and mechanical properties of the implant [31–34]. MgO is one of the primary constituents of bioglass and has antibacterial properties [35,36]. An improvement in the macrohardness, and yield and tensile strengths of Mg/MgO

composites that were reinforced by MgO nanoparticles have been reported [37] by Goh et al. The mechanical properties and corrosion resistance of a Mg-based metal matrix composite was enhanced by the addition of MgO ceramics as reinforcements through a PM technique [38]. Accordingly, the combination of a metallic matrix and MgO could allow the fabrication a metal matrix composite as a biomaterial capable of full degradation [38–40]. However, fabrication, and biodegradation behavior of Mg/HA/MgO nanocomposites have not been reported. In this study, pure Mg as the matrix material and HA and MgO nanoparticles as the reinforcements were selected to synthesis the Mg/HA/MgO bio-composite using the powder metallurgy method. In addition, the effects of various amounts of HA and MgO nanopowders on the microstructure, bio-corrosion behavior, physical properties and in vitro biocompatibility of the Mg-based bionanocomposite were investigated.

2. Materials and methods

2.1. Preparation of powder samples

Nano-powders of magnesium (Mg, 99.9% purity, 325 mesh), periclase nanopowders (MgO, 99.9%, average particle size <100 nm) and nano-hydroxyapatite (HA, Ca₁₀(PO₄)₆(OH)₂, 99.9% purity, average particle size <100 nm), which were supplied by SIGMA–ALDRICH, were used as the raw materials. Powder mixtures of four compositions: 72.5Mg–27.5HA, 75Mg–20HA–5MgO, 77.5Mg–12.5HA–10MgO, and 80Mg–5HA–15MgO (wt%) named samples MHM0, MHM5, MHM10 and MHM15, respectively, were dried in a vacuum dry oven at 220 °C for 10 h and subsequently mixed using a planetary ball mill for 2 h in an argon atmosphere. Uniaxial pressing was applied at a pressure of 840 MPa followed by sintering at the temperature of 400 °C for 1.5 h in argon atmosphere to fabricate cylindrical compacted specimens that were 12 mm in diameter and 5 mm in height as the substrate for the immersion, electrochemical and contact angle measurement tests.

2.2. Characterisation of powder samples

The XRD measurements of corrosion products were investigated using a Philips diffractometer with Cu K α radiation ($\lambda = 0.15406$ nm). The XRD pattern analysis was performed using the “MDI jade6” software. The XRD patterns were compared with standards compiled by the JCPDS standards. The following equation was used to determine the fraction of crystalline HA phase (crystallinity) from the XRD data [41]:

$$B_{\text{hkl}} \sqrt[3]{X_c} = K \quad (1)$$

where X_c is the fraction of the crystalline HA phase in corrosion products, K is a constant equal to 0.24 and B is the full width at half maximum (deg.) of selected reflection peaks. The structural features of the HA powders were repeated twice for two groups of peaks: one group was (002), (211) and (300) and the other group was (222), (004) and (213), the Miller planes family. The average of these two measured values was presented as the average fraction of the crystalline HA phase. The surface elemental composition and valance state of the surface elements of soaked samples in SBF solution were identified by X-ray photoelectron spectroscopy (XPS). The morphologies, particle sizes and composition were analyzed using field-emission scanning electron microscopy equipped with energy dispersive X-ray spectroscopy (FESEM, JEOL JSM 6380LA) and transmission electron microscopy (TEM, Philips CM10). AFM (SPI3800) was used to investigate of the growth morphology and roughness of the soaked samples in SBF solution.

Measurements of the surface area were made at three random sites of the same location of the samples. Static contact angles (CAs) with SBF and surface energy measurements were performed on a FTA200 drop shape analysis system at room temperature. The drop image was stored using a video camera, and the CAs were calculated from the shape of the drop using an image analysis system. The SBF drops were individually placed on each sample surface (0.6 μl /drop), and then, the corresponding CAs were measured. Six different regions on the surface of the samples before and after 7 days of immersion in SBF solution were used, and the measured results were averaged to reduce deviation.

2.3. Electrochemical tests

The electrochemical test was recorded at 37 °C in a glass cell containing 250 ml of Kokubo simulated body fluid (SBF) at pH ~7.5 using a Versastat3 potentiostat/gavanostat (Princeton Applied Research). Concentrated solutions of NaCl (8.037 g/L), NaHCO₃ (0.351 g/L), KCl (0.224 g/L), K₂HPO₄·3H₂O (0.231 g/L), MgCl₂·6H₂O (0.310 g/L), CaCl₂ (0.294 g/L), Na₂SO₄ (0.073 g/L), tri-hydroxymethyl aminomethane (CH₂OH)₃ CNH₂ (6.062 g/L) and 1.0 mol/L HCl (40 ml) were used for preparation of the SBF solution by pipetting the calculated amounts [42]. The exposed surface area of the tested specimens in SBF solution was 0.402 cm². Moreover, a saturated calomel electrode (SCE) and graphite rod were used as the reference and counter electrode, respectively, where the specimen was the working electrode in a three-electrode cell for the potentiodynamic polarisation tests. All of the experiments were recorded at a scan rate of 0.5 mV/s started at –250 mV_{SCE} below the open circuit potential. The software allows the ability to control this fitting manually. Selecting a segment of the curve from E_{corr} VSCE was performed for the Tafel fittings, and i_{corr} was subsequently estimated from the value, where the fit intercepted the potential value of the true E_{corr} VSCE [43]. The reproducibility of the results was verified by performing each experiment three times. All of the potentials were referred to the SCE.

2.4. Immersion tests

ASTM G31–72 standard was used to conduct the immersion tests of the specimens [19,44]. The rounded specimens with a size of 5 mm × Ø12 mm were ground with 400–2000 grit SiC papers. The specimens were then washed with distilled water, rinsed, ultrasonically degreased with ethanol, and dried at room temperature. The specimens were then immersed into a beaker containing 200 ml of Kokubo simulated body fluid (SBF). The beakers were sealed with a pH value of ~7.5 and incubated at a constant temperature of 37 °C for 3, 7 and 14 days. Afterwards, the specimens were rinsed with acetone and deionised water, and the corrosion products were removed with a chromate acid solution (200 g/L CrO₃ + 10 g/L AgNO₃) before weight measurement. The weight loss rate was calculated as follows [38]:

$$C_R = \frac{W}{At} \quad (2)$$

where C_R is the corrosion rate, W is the weight loss, A is the surface area exposed to the corrosive media and t is the exposure time. A 168 h immersion in the SBF solution was employed to measure the released hydrogen amount from the samples. A sample was immersed in a beaker that was covered with a funnel to collect the evolved hydrogen in a burette above the funnel. The hydrogen amount was calculated in ml/cm² prior to renewing the solution, and the volume of hydrogen was measured with a scaled burette. The average pH value of the SBF from three measurements was

recorded during the soaking experiment after an interval of 12 h.

2.5. Cell culture

Cell viability was investigated by using of the seventh passage of the normal human osteoblasts (NHOst) cells cultured in an osteoblast basal medium (OBM), with the osteoblast growth medium (OGM), which supplemented with 0.1% ascorbic acid, 10% Fetal Bovine Serum (FBS), and 0.1% of gentamycin. They were then put in an incubator under cell culture conditions (90 ± 2% humidity, 37 ± 1 °C, 5% CO₂, and 20% O₂). The sample sterilization in a steam autoclave at 120 °C for 30 min was followed by 1 h ultraviolet (UV) irradiation. The mixed samples with the OBM were then kept in an incubator with atmosphere of 5% CO₂ for 72 h at 37 °C. Following incubation, a 0.20 μm membrane filter was used to filter the extracted samples that stored at 4 °C, prior to use.

2.6. Cell viability testing and ALP activity

The indirect contact was used to perform the cell viability test by using the MTT (3-(4, 5-Dimethylthiazol-2-yl)-2,5-Diphenyltetrazolium Bromide) assay (Invitrogen, M6494); 1.5 × 10⁴ NHOst cells were seeded in each well of a 96-well plate for 24 h, and then the media were replaced with the sample extracts after 3, 7 and 9 days. The culture medium was aspirated and the samples were washed twice with PBS after the incubation, and then 100 μl of fresh medium was added to each well. Following this, 10 μl of MTT were added to each well and incubated for 4 h. After incubation, the medium was aspirated and 100 μl of dimethyl sulfoxide (DMSO; stock solution) were added to each well, and absorbance was measured at 540 nm using an automated microplate reader (Tecan, Safire²).

The ALP activity, which is an important component for bone formation, was measured by analyzing the cells differentiation of NHOst cells [45]. The cells were cultured on MHM0, MHM10 and MHM15 specimens for 3, 7 and 9 days to observe the activity of alkaline phosphatase. Alkaline phosphate yellow (pNPP) liquid substrate system for ELISA (Sigma, USA) was used for measuring ALP activity. After 3 days of the cell culture, the MHM samples were washed thrice with PBS. Then 400 μl of p-nitrophenylphosphate (pNPP, pH 9.8) liquid was added to the MHM samples and incubated for 30 min at 37 °C till the color of solution becomes yellow. The enzyme reaction was terminated by an addition of 1.5 ml of 0.6 N NaOH and the absorbance of p-nitrophenol (pNP) was read in spectrophotometric plate reader at 540 nm. The value obtained from the medium with levamisole was subtracted from that without levamisole as a background level. The data were analyzed via SPSS v.16.0 and repeated measures of analyses of variance (ANOVA) test were done followed by post-hoc Least Significant Difference (LSD), with the significant level set at a p-value less than 0.05. Four to five samples were used for each MHM nanocomposites for MTT-assay and ALP activity tests. For MTT-assay the triplicates were carried out, as well as the percentage of cell viability was calculated using the following formula:

$$\text{Cell Viability (\%)} = \frac{OD_{\text{sampe}} - OD_{\text{blank}}}{OD_{\text{control}} - OD_{\text{blank}}} \times 100\% \quad (3)$$

2.7. Mechanical and physical testing

The final milled powder samples were cold compacted in the form of a pellet with a size of 24 mm × Ø12 mm (according to ASTM E9 standard [46]) in a polyurethane mold using a cold isostatic

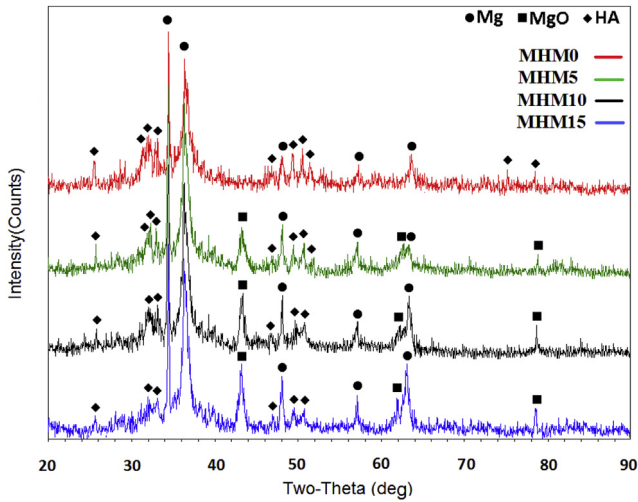


Fig. 1. XRD patterns of the MHM samples after blend-cold press-sinter process.

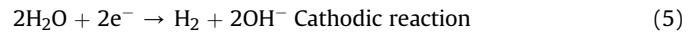
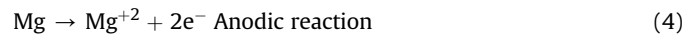
press (CIP 32260, Avure Autoclave) operated at an optimized load of 414 MPa for 5 min. The compacted pellets were sintered at an optimized temperature of 400 °C for 2 h under argon atmosphere to obtain an envelope density closer to the absolute density. The uniaxial compression testing was conducted with an Instron 3365 testing machine at a constant nominal strain rate of 1 mm/min at the room temperature. The ultimate compressive strength UCS (MPa), and compressive failure strain ϵ (%) were defined. The Archimedes water immersion method was employed to measure density. Five identical samples were used for the compression

testing and density measurements of each sample then the average values were reported.

3. Results and discussion

3.1. Microstructure, electrochemical and immersion measurements

The XRD patterns of MHM nanocomposites after mechanical milling, pressing and sintering are shown in Fig. 1. The characteristic sharp peaks of Mg were detected in the XRD patterns of the as-received material, whereas MgO and HA were characterized by smaller and broader XRD peaks. Fig. 2 shows the distribution of powder particles in MHM0 and MHM10 samples. As can be seen from the figure, increasing the HA content from 12.5 wt% (MHM10) to 27.5 wt% (MHM0), caused an increase in HA agglomerates (the black spots). Moreover, the number of pores/voids around and inside the HA agglomerates (Fig. 2d) increased by increasing of HA content. The elemental mapping of different elements in the matrix of the MHM0 sample confirmed the presence of HA agglomerates (Fig. 2e–h). The polarization curves of the MHM samples soaked in SBF solution showed in Fig. 3. Additionally, the dissolution of Mg is shown by the anodic polarization curves, and the cathodic polarization curves show the hydrogen evolution [47]:



The current density of the Mg/27.5 wt% HA nanocomposite significantly increased and quickly reached its limiting value of $\sim 420 \mu\text{A}/\text{cm}^2$, which shows the high corrosion rate of the MHM0

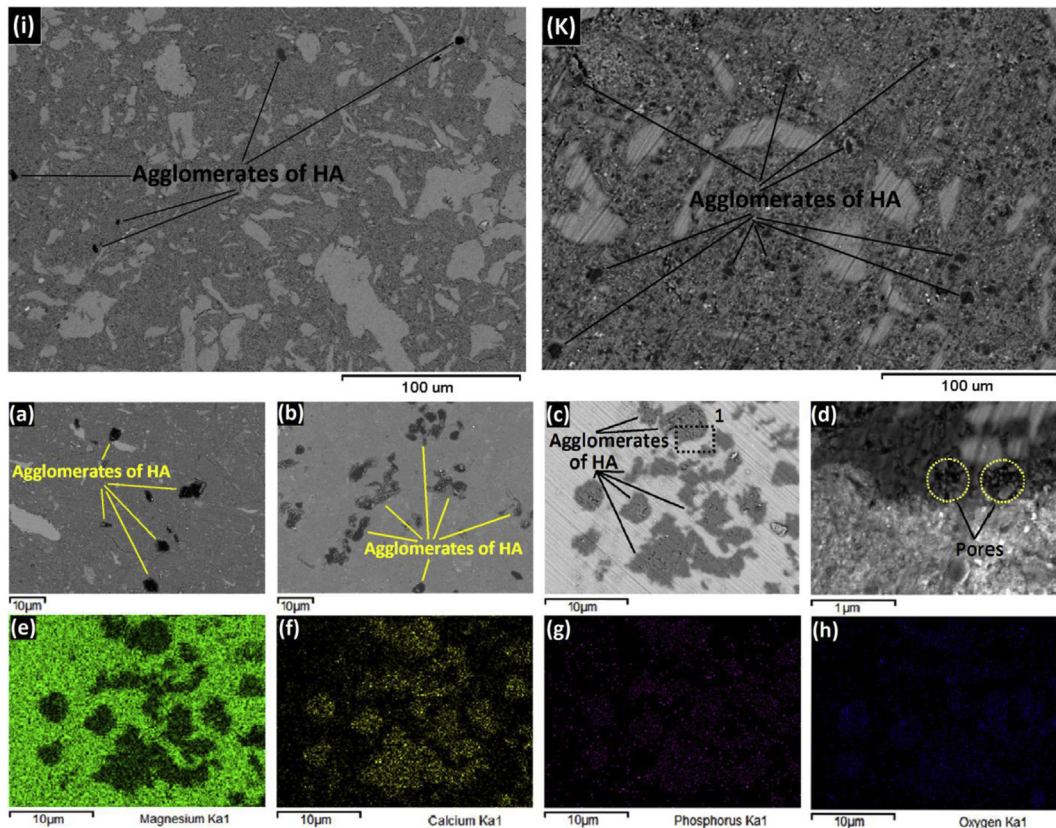


Fig. 2. FESEM images of the (a and i) MHM10, (b, c and j) MHM0 nanocomposites and (d) high magnification of area 1 in (c). (e–h) X-ray map of (c).

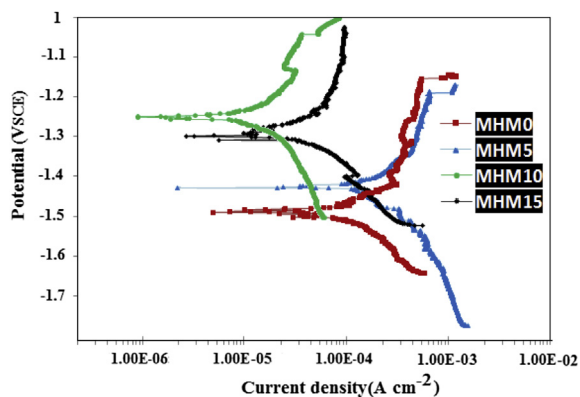


Fig. 3. Potentiodynamic polarization curves of the MHM0, MHM5, MHM10 and MHM15 specimens in the SBF solution.

sample in the initial stage of the electrochemical test (based on Formula (6)) according to the anodic branches in polarization curves (Fig. 3). As a passivity region was reached, the anodic polarization curve of the MHM0 sample tended to stabilize; then the slope of anodic curve increased due to the decrease in the Mg dissolution rate. By the following equation, the corrosion rate (P_i) calculated using the corrosion current density, i_{corr} (mA/cm^2) [48,49]:

$$P_i = 22.85i_{corr} \quad (6)$$

The passivity regions on the anodic polarization curves can be attributed to the formation of corrosion products as the protective coverage forms. The breakdown and reformation of the corrosion product films during immersion in the SBF solution can create the fluctuations in the anodic polarization curves (Fig. 3). In addition, the formation of corrosion pits on the soaked samples can indicate these fluctuations in the anodic branch. Table 1 lists the corrosion current density (i_{corr}), corrosion potential (E_{corr} , V_{SCE}), pitting corrosion potential (E_{pit}), cathodic Tafel slopes (β_c), anodic Tafel slopes (β_a) and corresponding corrosion rate (P_i) of the specimens extracted from the polarization curves. In addition, the polarization resistance (R_p) of the MHM samples was calculated using the electrochemical parameters (i_{corr} , β_a and β_c) based on the following equation [48]:

$$R_p = \frac{\beta_a \beta_c}{2.3(\beta_a + \beta_c)i_{corr}} \quad (7)$$

By decreasing the HA content to 20 wt% and adding MgO up to a content of 5 wt% in the raw material MHM samples, the current density showed no considerable change, while the electrochemical potential shifted to a more noble region, which shows the improvement in the corrosion behavior of the MHM5 sample compared to that of the MHM0 sample. The cathodic slope of the

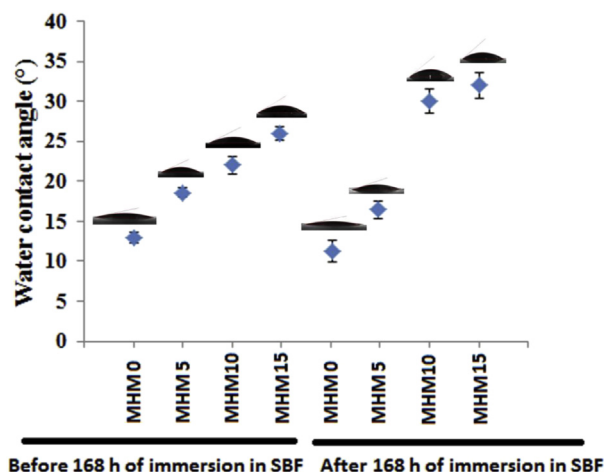


Fig. 4. Water contact angle measurements of MHM samples before and after 168 h of immersion in a SBF solution at 37 °C.

MHM5 sample decreased compared to that of the MHM0 sample, which indicates a decrease in the hydrogen evolution rate of the MHM5 sample. Additionally, the polarization resistance improved from $0.25 \text{ k}\Omega \text{ cm}^2$ in the MHM0 sample to $0.29 \text{ k}\Omega \text{ cm}^2$ in the MHM5 sample. Although, a significant decrease was observed in the current density of the MHM10 sample ($46.8 \mu\text{A}/\text{cm}^2$) when the MgO content was increased to 10 wt%, and the HA content was decreased to 12.5 wt%; moreover, the electrochemical potential increased to -1258.2 mV_{SCE} , which is significantly higher than those of the MHM0 (-1487.3 mV_{SCE}) and MHM5 (-1434.6 mV_{SCE}) samples. The decrease in the current density and the considerable increase in the electrochemical potential of polarization curves indicate the enhancement in the corrosion behavior of MHM10 sample compared to those of the MHM0 and MHM5 samples. This improvement in the corrosion behavior of the MHM10 sample can be attributed to the decrease in the number of pores and voids around the HA agglomerates (Fig. 2) caused by the decrease in the HA content from 27.5 to 12.5 wt% in the raw material. Less penetration of the corrosive solution into the matrix of the MHM10 nanocomposite was yielded by the presence of fewer numbers of pores and voids in the matrix of the nanocomposite. As a result, the polarization resistance of the MHM10 sample increased, and its corrosion rate decreased compared to those of the MHM0 and MHM5 samples (Table 1). According to the wettability measurements, the penetration of the SBF solution was lower in the surface of nanocomposites with lower amounts of HA in the raw material (Fig. 4).

By decreasing the HA content to 5 wt% and increasing the MgO content to 15 wt% in the raw material, the current density of the polarization curve of the MHM15 sample was found to increase, while the electrochemical potential decreased compared to those of the MHM10 sample, indicating that the decrease in the corrosion

Table 1
Electrochemical parameters of MHM samples in SBF solution attained from the polarisation test.

Sample	Corrosion potential, E_{corr} (mV vs. SCE)	Current density, i_{corr} ($\mu\text{A}/\text{cm}^2$)	Cathodic slope, β_c (mV/decade) vs. SCE	Anodic slope, β_a (mV/decade) vs. SCE	Polarization resistance, R_p ($\text{k}\Omega \text{ cm}^2$)	Corrosion rate, P_i (mm/year)
Mg-27.5%HA	-1487.3	187.4	411.2	149.6	0.25	4.28
Mg-20%HA-5% MgO	-1434.6	203.6	344.9	235.3	0.29	4.65
Mg-12.5%HA-10%MgO	-1258.2	46.8	200.8	391.4	1.23	1.06
Mg-5%HA-15% MgO	-1293.8	85.2	288.5	330.7	0.78	1.94

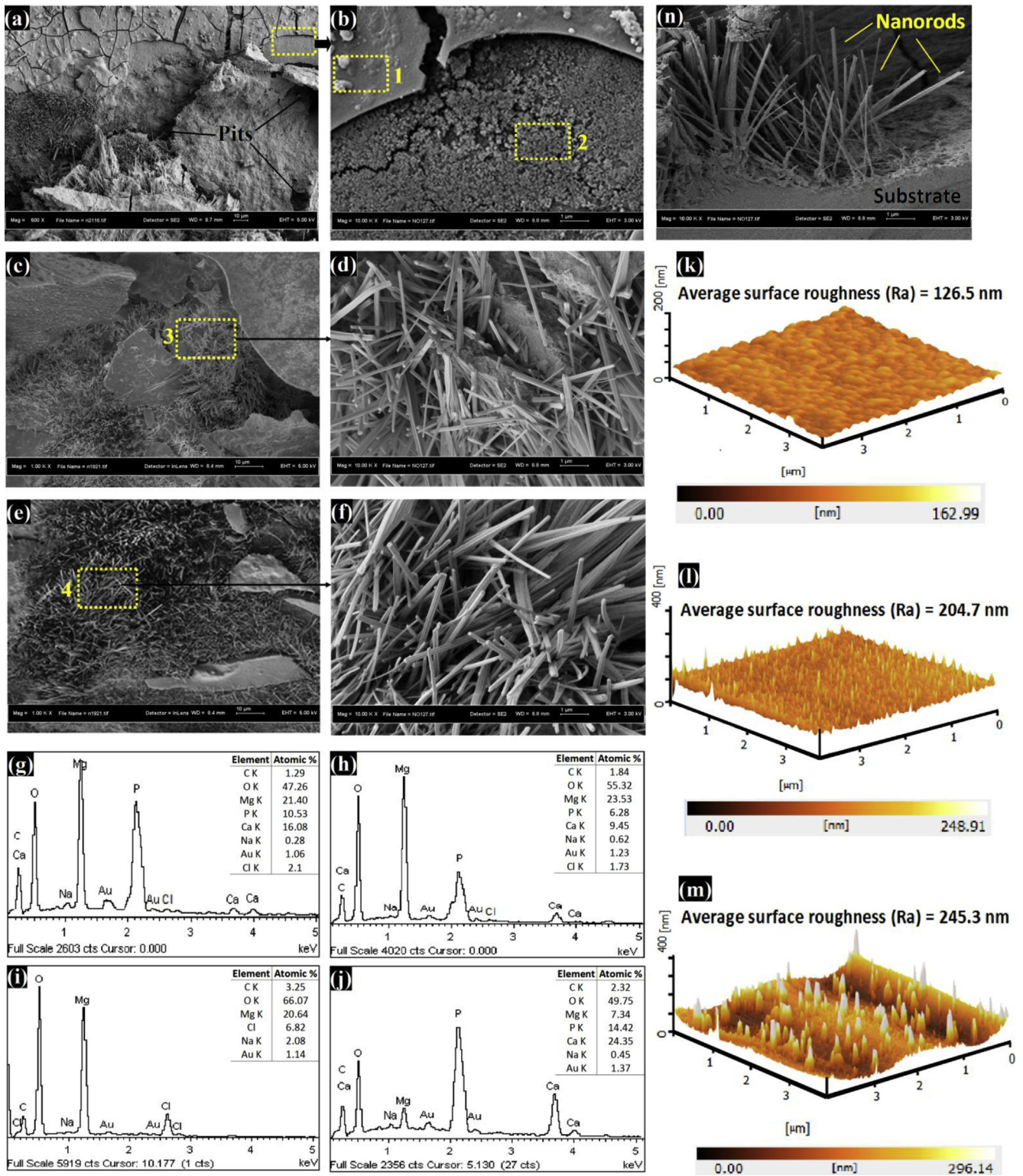


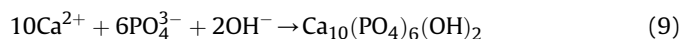
Fig. 5. FESEM images of (a, b) the MHM0, (c, d) MHM10, (e, f) MHM15 specimens and (n) cross-section of MHM10 after 168 h of immersion in a SBF solution at 37 °C. EDS analyses of (g) area 3 in (c), (h) area 4 in (e), (i) area 2 in (b), and (j) area 1 in (b). 3D-AFM image of (k) the MHM0, (l) MHM10, and (m) MHM15 specimens after electrochemical tests in a SBF solution.

resistance of the MHM15 sample. In addition, the decrease in the HA content of the matrix of the nanocomposite can cause the decrease in the polarization resistance and the increase in the corrosion rate of the MHM15 sample compared to those of the MHM10 sample. As a result, the presence of HA in the raw material

has two different effects on the corrosion behavior of the nanocomposites: Firstly, because of the less solubility of HA than Mg, the corrosion resistance of magnesium-based nanocomposites improved by the addition of HA [18,39]. Secondly, the pores and voids that formed around the HA agglomerates increased the

penetration of the corrosive media in the matrix of the nanocomposites, causing the corrosion behavior of the samples to decrease by increasing the HA content in the raw material. The formation of HA agglomerates during the fabrication of Mg/HA composites have also been reported by Witte et al. [18] and Gu et al. [19]. As a result, a suitable method to optimize the corrosion behavior of Mg/HA-based composites is using an optimum amount of HA in the raw material. Additionally, the nucleation of the CaP compound on the surfaces of the samples was stimulated during immersion in the physiological solution by the presence of HA in the matrix of the nanocomposite, which can improve the bioactivity and biocorrosion behavior of the samples. A higher hydrogen evolution rate in the MHM15 sample compared to that of the MHM10 sample can be indicated by the increase in the cathodic branch slope of the MHM15 sample. The fluctuations in the passivity region of the anodic branch approximately disappeared in the MHM15 sample, indicating a decrease in the pitting corrosion of this sample compared to the other samples.

Weight loss tests were performed by immersion of the MHM samples in the SBF solution at 37 °C for 3, 7 and 14 days to further investigate the corrosion mechanism and to calculate the weight loss rate of the MHM samples. After 7 days of immersion in the SBF solution, the morphology and composition of the corrosion products that were deposited on the surface of the Mg/HA/MgO nanocomposites were investigated by TEM and FE-SEM analysis. Fig. 5 shows the low- and high-magnification FE-SEM images of the MHM samples immersed in SBF for 7 days and the corresponding EDS analysis of the chemical composition of the corrosion products. Severe corrosion attack was observed in the MHM0 sample (Fig. 5a). The corroded surface was divided into two regions to better describe the corrosion mechanism: (1) the smooth and slightly corroded region, which showed a web-like morphology; and (2) the severely corroded region, which contained accumulated corrosion products (Fig. 5a and b). Localized regions showing severe corrosion exhibited some pits and deep cracks, which tend to become channels for the penetration of the physiological solution, leading to further corrosion of the Mg-27.5%HA nanocomposite substrate. In addition, accumulation of a large amount of corrosion products on the MHM0 sample was observed after 7 days of soaking in the SBF solution. The magnified FE-SEM image of the slightly corroded region (Fig. 5b) shows that the outer layer has a web-like morphology consisting of hemispherical domes and microcracks that cover the smooth underneath layer. The web-like film precipitated on the MHM0 sample was primarily composed of Ca and P, while the layer beneath was rich in Mg and O. The Ca/P ratio measured on the web-like films was ~1.6, which is close to the Ca/P ratio of HA [50]. CaP compounds such as HA formed on the surface of the samples by the reaction of phosphate ions (HPO_4^{2-} or PO_4^{3-}) and Ca^{2+} with OH^- ions in the SBF solution after different immersion times based on reactions 8 and 9 [38,39]:



The corrosion products of the Mg alloys in the simulated body fluid were composed of magnesium oxide or magnesium hydroxide and calcium phosphate (CaP) compounds as assumed by Witte et al. [18]. Thus, the formation of $\text{Mg}(\text{OH})_2$ and CaP compounds as the protective layers is reasonable in this study. During the soaking of the MHM0 sample in SBF solution, the number of corrosion pits and deep cracks (Fig. 5a) increased the penetration of the corrosive media that reacted with the substrate, producing higher amounts of $\text{Mg}(\text{OH})_2$ and hydrogen gas based on reaction (9) [51]:



The number of corrosion pits increased by the release of a higher amount of hydrogen gas; widened the gap between the cracks; and damaged the protective layers made of the corrosion products, such as CaP compounds and $\text{Mg}(\text{OH})_2$. The vertical growth of nano-rods and some narrow cracks appeared on the surface of the MHM10 and MHM15 nanocomposites, after 7 days of immersion in the SBF solution (Fig. 5c–f). Based on the EDS analysis, the nanorods can be related to the $\text{Mg}(\text{OH})_2$ and/or MgO phases, while the atomic percentage of Ca, P and Cl elements decreased in the corrosion products of the MHM10 sample compared to those of the MHM0 nanocomposite. The hydrothermal condition of immersion in the SBF solution at 37 °C in addition to the presence of MgO nanoparticles in the raw material of the MHM10 and MHM15 samples led to the nucleation and growth of $\text{Mg}(\text{OH})_2$ nanorods during the 7 days of immersion based on reaction (11):



After 7 days of immersion in the SBF solution, some films of the CaP compound were observed in the corrosion products of the MHM10 sample based on the FE-SEM micrographs and the corresponding EDS analysis. The surface of the MHM15 sample with 15 wt% of MgO in its raw material covered with the nanorods (Fig. 5e and f). However, the diameter of the nanorods in the corrosion products of the MHM15 sample increased compared to that of the MHM10 sample.

The Ca/P ratio found on the corrosion products of the MHM10 and MHM15 samples was approximately 1.5, which indicates the presence of a higher amount of $\text{Ca}_3(\text{PO}_4)_2$ in the corrosion products compared to the HA amount [50,52]. However, the Ca/P ratio measured on the corrosion products of MHM5 sample was ~1.6, which is near the Ca/P ratio of HA [50]. After 3, 7 and 14 days of immersion in the SBF solution at 37 °C, degradation and weight loss analysis were performed in all MHM samples. The results are shown in Fig. 6; the weight loss rates were obtained by the weight loss amounts based on Eq. (2). As seen, the results of the immersion tests are consistent with those of the electrochemical measurements, indicating the effective enhancement of the corrosion behavior of the samples due to the addition of MgO and the decrease of the HA content in the raw material of the Mg/HA/MgO nanocomposites. The weight loss rate of the MHM0 sample was considerably higher than those of the MHM10 and MHM15 samples (Fig. 6). After immersion in the SBF for 72 h, the weight loss rate of

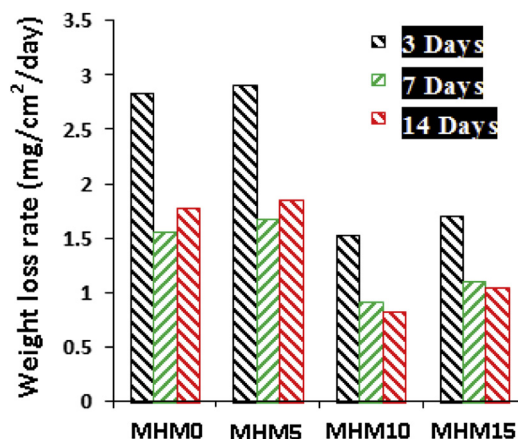


Fig. 6. Corrosion rate obtained by weight loss of MHM samples in SBF solution for duration of 3, 7 and 14 days.

the MHM0, MHM5, MHM10 and MHM15 samples were 2.84, 2.91, 1.53 and 1.7 mg/cm²/day, respectively. During the first 72 h of immersion, the weight loss rate increased in all MHM samples, whereas it rapidly decreased from 72 to 168 h of immersion in SBF solution (Fig. 6). The protection against corrosion attacks can be occurred by the formation of corrosion products such as Mg(OH)₂ and CaP compounds on the immersed samples that decreased the weight loss rate of the MHM samples. However, the weight loss rates of the MHM0 and MHM5 samples gradually increased during the remainder of the immersion experiments up to 336 h, which indicates the destruction and dissolution of the corrosion products. For example, by increasing the immersion time, the chloride ions (Cl⁻) of the SBF solution would react with Mg(OH)₂ to form a more resolvable MgCl₂ (reaction 12), so that the protective films made of Mg(OH)₂ were destroyed, exposing the deep uncorroded nanocomposite substrate to the corrosive solution and thus increasing the weight loss rate of the samples [39,53].



Conversely, by increasing the immersion time from 168 to 336 h, the weight loss rate of the MHM10 and MHM15 samples decreased, which demonstrates the stability of the corrosion products of these samples against degradation. Based on the FE-SEM images of the corrosion products, after 7 days of immersion in SBF, the formation of Mg(OH)₂ nanorods as a protective layer on the surface of the MHM10 sample could enhance the degradation behavior of the MHM10 sample. The decrease in the weight loss rate of the MHM15 sample by increasing the MgO content in the raw material of the nanocomposite up to 15 wt% could be attributed to the nucleation of more nanorods on the MHM15 sample, which confirms the positive effect of the formation of Mg(OH)₂ nanorods to protect the MHM samples from aggressive solutions during 7 days of immersion in the SBF solution. However, based on the EDS analysis, the formation of a smaller amount of CaP compounds on the surface of the MHM15 sample compared to that of the MHM10 sample caused the weight loss rate of the MHM15 sample showed higher amount. Moreover, after 7 days of immersion, a lower amount of Cl was observed in the corrosion products of the MHM10 and MHM15 samples compared to those of the MHM0 sample based on EDS analysis. Therefore, a lower amount of MgCl₂ was formed in the MHM10 and MHM15 samples, which demonstrates the stability of the Mg(OH)₂ nanorods to transformation (12). Thus, the stability of the Mg(OH)₂ nanorods against degradation might decrease the weight loss rate of the MHM10 and MHM15 samples compared to that of the MHM0 and MHM5 samples after 14 days of immersion in the SBF solution.

The wettability of the MHM samples decreased by increasing MgO to 10 wt% and by decreasing HA to 12.5 wt% in the raw material of the nanocomposites according to the contact angle measurements that were performed on the soaked samples after 7 days of immersion in the SBF solution (Fig. 4). The decrease in wettability of the soaked samples can be attributed to the composition and/or morphology of the corrosion products. For example, the contact area between the substrate and the physiological solution can be decreased by the vertical growth of the Mg(OH)₂ nanorods with a hierarchical microstructure on the surface of the soaked samples. Consequently, the contact angles and thus the wettability of the MHM10 and MHM15 soaked samples, which contained higher amounts of Mg(OH)₂ nanorods, decreased compared with those of the MHM5 and MHM0 soaked samples. Additionally, the wettability of the soaked samples can be affected by the formation of cracks and pits on the samples during the 7 days of immersion in the SBF solution. Based on the weight loss rates and the contact angle measurements, the wettability affects the degradation

behavior of the samples because higher contact angles with SBF drop indicates lower penetrations of the media solution into the MHM samples during immersion.

Fig. 7 indicates the correlation between the surface energy, corrosion rate and weight loss rate of MHM samples. According to the Fig. 7, the surface energy of MHM15 and MHM10 samples indicated smaller values than that of the MHM0 and MHM5 samples. As reported by Song and Xu [48], the electrochemical dissolution rate of AZ31 Mg alloy decreased by decreasing of the surface energy value. Yong et al. have also reported that the activation energy of corrosion was gained by the surface energy of samples [53]. Therefore, decrease in the surface energy value of MHM15 and MHM10 samples compared to the MHM0 and MHM5 samples can be a reason to decrease of the corrosion rate and weight loss rate of MHM15 and MHM10 samples. Additionally, the reduce in surface free energy and wettability of a magnesium alloy to improve corrosion behavior have been performed by plating of the polymeric nanofilms on the sample surface [54]. Fig. 8 shows the change in the pH of the SBF solution measured during the immersion of the MHM samples as a function of the immersion time. A linear increase in the pH of the SBF solution was found with the MHM samples during the initial periods of immersion (e.g., up to ~48 h), increasing with the immersion time due to the fast degradation of Mg based on reactions (3) and (4). The rate of increase in the pH of the SBF solution reduced by further increases in the immersion time (e.g., above ~48 h), which could be attributed to the formation of Mg(OH)₂ on the surface of the MHM samples as protective coverage. However, the presence of higher concentrations of highly corrosive chloride ions from NaCl, KCl and CaCl₂ in the SBF solution is likely to promote the formation more resolvable MgCl₂ based on reaction (12); as a result, Mg(OH)₂ dissolved with a

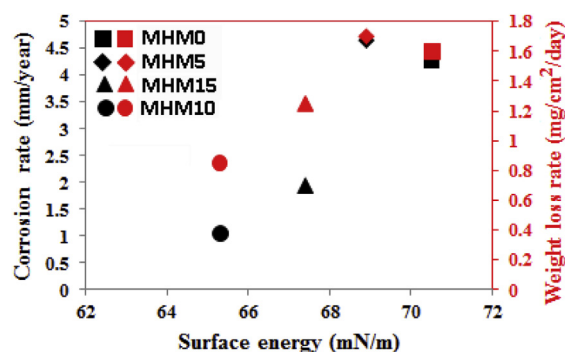


Fig. 7. The surface energy of MHM samples versus the corrosion rate and weight loss rate of the MHM samples.

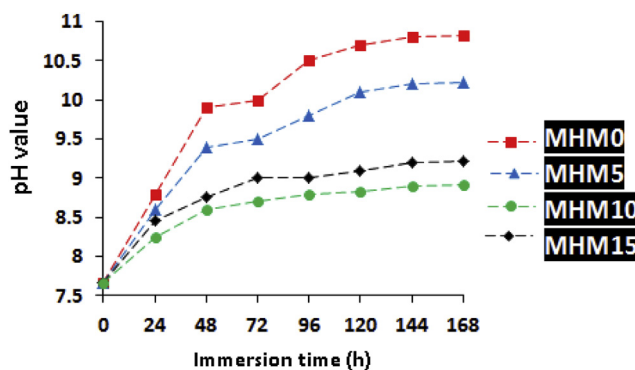


Fig. 8. Change in pH of the SBF solution during immersion of MHM specimens for duration of 168 h.

corresponding increase in the pH of the SBF solution from ~72 h to ~120 h of immersion time due to the release OH^- ions. When $\text{pH} > 10$ in the SBF solution, attack of the chloride ions on $\text{Mg}(\text{OH})_2$ intensified in interfacial region [53].

During 72–120 h of immersion, the rate of increase in the pH of the SBF solution with time with the MHM10 and MHM15 samples were significantly lower than those of the MHM0 and MHM5 samples, which could be attributed to the increased stability of these samples and their corrosion products against the degradation by the aggressive solution. By continuing the immersion time above ~120 h, the increase in the accumulation of $\text{Mg}(\text{OH})_2$ and the formation of HA via the consumption of OH^- ions based on reactions (8) and (9) decreased the dissolution kinetics; thus, the rate of increase in the pH of the SBF solution was restricted, and eventually, the pH values reached saturation. The pH of the SBF solution with the MHM10 and MHM15 samples reached saturation after ~96 h of immersion and remained in the same range until 168 h of immersion, which demonstrated the protection of these samples by their corrosion products. In addition, based on the contact angle measurements, the vertical growth of the $\text{Mg}(\text{OH})_2$ nanorods in their hierarchical microstructure decreased the contact area between the SBF solution and the substrate of the MHM10 and MHM15 samples; the release of hydroxide ions by the degradation of the substrate was thus restricted, and as a result, the pH of the SBF solution remained relatively constant by increasing of the immersion time to 168 h.

The hydrogen evolution results of the MHM samples in the SBF solution for 168 h of immersion showed in Fig. 9. The contact area of samples with corrosive solution was decreased by the formation of the corrosion products on the samples that caused the hydrogen volume released from the MHM samples to decrease when the immersion time increased from ~72 h to ~96 h. However, by increasing the immersion time, the hydrogen evolution rate of the MHM0 and MHM5 samples increased due to the destruction and degradation of their corrosion products, and as a result, the penetration of the corrosive solution increased in the substrate nanocomposites, which intensified the dissolution of Mg. With the addition of MgO and the reduction of HA in the raw material of the nanocomposites, the hydrogen volume released from the MHM samples decreased due to the slower hydrogen evolution and the lower rate of Mg dissolution. The decrease in the wettability of the MHM10 and MHM15 samples due to the decrease in the number of pores around the HA agglomerates as well as, the formation and vertical growth of the $\text{Mg}(\text{OH})_2$ nanorods during immersion in the SBF solution caused a smaller amount of corrosive solution to

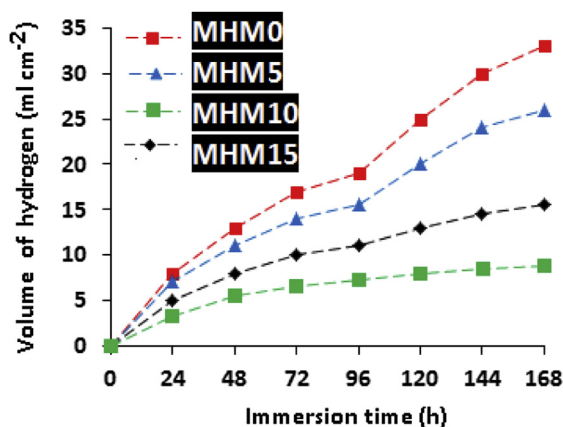


Fig. 9. Hydrogen evolution during immersion of the MHM specimens in the SBF solution for duration of 168 h.

penetrate into their substrate; thus, a lower volume of H_2 was released by the degradation of Mg based on the reactions (4) and (5) compared to that of the MHM0 and MHM5 samples.

AFM images of the MHM samples after the electrochemical test in the SBF solution showed in Fig. 5. As shown, after the electrochemical test in the SBF solution, the micro hemispherical domes were formed on the surface of the MHM0 sample. However, the nano-rods were nucleated and grew vertically in some parts of the MHM10 sample. As shown in Fig. 5k, the surface roughness average (Ra) value of the MHM0 sample was calculated to be 126.5 nm; however, this value increased to 204.7 nm in the MHM10 sample (Fig. 5l). The diameter of the nanorods increased by increasing of amount of MgO nanoparticles to 15 wt% in the raw material of the nanocomposites, as well as the formation and growth of the nanorods increased the surface roughness of MHM15 sample (245.3 nm) compared to that of the MHM0 and MHM10 samples after the electrochemical test in the SBF solution (Fig. 5m). Additionally, a considerable increase in the corrosion resistance of the coated samples due to increasing surface roughness was reported in recent studies [31,54]. The immersion of the specimens caused the Mg and MgO components of the samples to react with the SBF solution; thus, $\text{Mg}(\text{OH})_2$ formed on the sample surface based on reactions (10) and (11). Therefore, the synthesis of the nano-rods on the surface of the MHM samples during the electrochemical test is composed of the $\text{Mg}(\text{OH})_2$ phase. In addition, by increasing the amount of MgO in the raw material of the nanocomposites, the synthesis of the $\text{Mg}(\text{OH})_2$ nano-rods based on reaction (11) was increased in the MHM samples, which was confirmed by the AFM images. The phase analysis of the corrosion products based on the X-ray diffraction patterns of the MHM samples after 168 h of immersion at 37 °C in the SBF solution showed in Fig. 10. During the immersion of the specimens, the Mg and MgO components of the samples reacted with the SBF solution; therefore, $\text{Mg}(\text{OH})_2$ formed on the sample surfaces based on reactions 9 and 10 [39]. In addition, based on the X-ray diffraction pattern of the immersed samples, a larger amount of $\text{Mg}(\text{OH})_2$ formed on the samples due to the increase in the amount of MgO in the raw material of the nanocomposite [39]. However, the chloride ions (Cl^-) of the SBF solution reacted with $\text{Mg}(\text{OH})_2$ to form a more soluble MgCl_2 via reaction (12) by continuing the immersion of the samples in the SBF solution. Therefore, after 7 days of immersion in the SBF solution, the MgCl_2 peaks were observed in the X-ray patterns of immersed samples. However, the number and intensity of XRD peaks of MgCl_2 decreased by increasing the amount of MgO in the nanocomposites, confirming the stability of the $\text{Mg}(\text{OH})_2$ nanorods against reaction (12). Based on the XRD patterns, the presence of phosphate ions (HPO_4^{2-} or PO_4^{3-}) and Ca^{2+} in the SBF solution and the reaction of

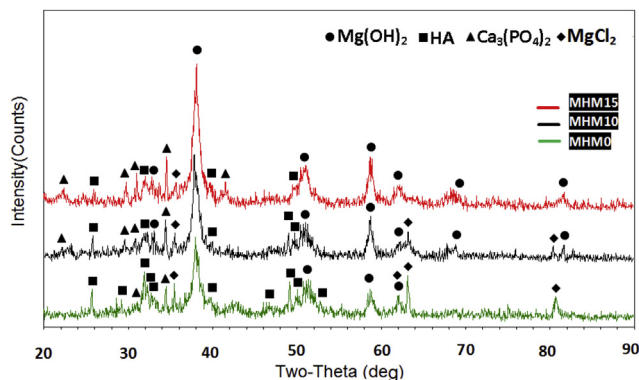


Fig. 10. XRD patterns of the MHM samples after 168 h of immersion in a SBF solution at 37 °C.

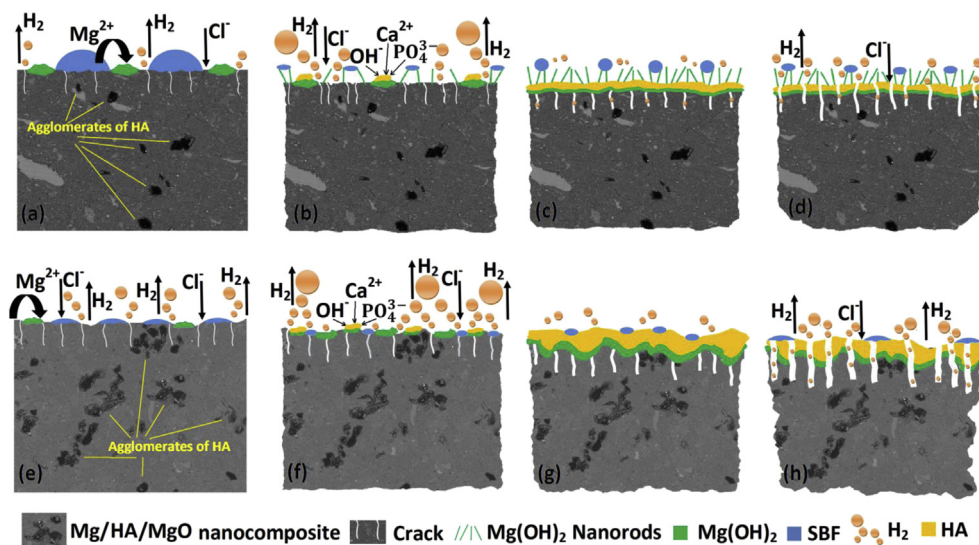


Fig. 11. Schematic illustration of the degradation mechanism of (a–d) MHM10 and (e–h) MHM0 samples in SBF solution.

these ions with OH⁻ ions formed HA on the surface of the specimens after 7 days of immersion based on reactions 7 and 8 [38,39]. By increasing the HA content in the raw material of the nanocomposites, the intensity of the XRD peaks of HA in the corrosion products increased due to the larger amount of OH⁻ released from the MHM0 sample compared to that from the MHM10 and MHM15 samples; this resulted in the formation of more HA on the MHM0 sample based on reactions (8) and (9) during immersion.

By immersion of MHM samples in SBF solution, the nucleation of more HA on the MHM0 and MHM5 samples compared to the MHM10 and MHM15 samples can be attributed to the presence of a larger number of HA nanoparticles in the raw material of the MHM0 and MHM5 samples. However, after 7 days of immersion in SBF, the spectra of Ca₃(PO₄)₂ appeared in the X-ray patterns of the corrosion products of the MHM10 and MHM15 samples, indicating the precipitation of Ca₃(PO₄)₂ instead of HA (reaction 13) onto these samples due to the release of a smaller number of OH⁻ ions in the SBF solution with the MHM10 and MHM15 samples.



The smaller release of OH⁻ ions from the MHM10 and MHM15 samples compared to that of the MHM0 sample confirmed the lower degradation rate of the MHM10 and MHM15 samples and could confirm the higher stability of Mg(OH)₂ with the rod-like morphology in the corrosion products of these samples. The corrosion mechanism of the MHM0 and MHM10 specimens is schematically illustrated in Fig. 11.

As shown in Fig. 11a and e, the wettability of the MHM samples decreased by increasing MgO to 10 wt% and by decreasing HA to 12.5 wt% in the raw material of the nanocomposites. The decreased wettability led to the reduction of penetration of SBF in MHM10 compared to the MHM0 sample. The increase in dissolution of Mg together with an increase in the evolution of H₂, which caused by the penetration of more amount of SBF in MHM0 substrate, intensifying the destruction of MHM0 surface during immersion in SBF solution. Fig. 11b and f shows the corrosion products such as Mg(OH)₂ and CaP compounds formed on the MHM0 and MHM10 samples. The growth of Mg(OH)₂ nanorods with a hierarchical microstructure decreased the surface contact area of MHM10 sample with SBF solution (Fig. 11b–d), thus decreasing its degradation rate. More corrosion products precipitated on the MHM0

than those of MHM10 sample, which can be attributed to the higher corrosion rate of MHM0 sample consisting more HA in its raw material (Fig. 11c and g). However, the corrosion film covering the surface of both samples was destroyed from the evolution of H₂ resulting in a fresh substrate surface getting the exposure to the SBF solution (Fig. 11d and h). As a result, the degradation of MHM samples intensified with immersion time.

In addition, to determine the effect of the composition of the raw material on the crystallinity of HA in the corrosion products, XRD profiles were used to evaluate the crystallinity of HA in the MHM samples. The decrease of HA in the raw material of the samples caused the crystallinity of the deposited HA on the soaked samples in SBF to decrease gradually from 32.67% in the MHM0 sample to 28.45, 24.36, and 21.33% in the MHM5, MHM10 and MHM15 samples, respectively. Generally, the fractional control of crystalline HA is required for biological applications. Because the high crystallinity of HA results in low activity towards bioresorption, and because HA is insoluble in a physiological environment, the high crystallinity of HA is preferred for dental applications. However, a lower degree of crystallinity of HA can be used to promote osteointegration or as a coating to advance bone growth into prosthetic implants [41]. The morphology and microstructure of the corrosion products that formed on the surface of the MHM samples after 7 days of immersion in the SBF solution were further examined via transmission electron microscopy (TEM) and selected area electron diffraction (SAED) and presented in Fig. 12. SAED patterns was used to calculate the inter planer spacing 'd' by a TEM image analysis software (Digital Micrograph- Gatan); the average of d-values were determined and the crystallographic planes corresponding to each ring was identified by comparing with the d-values extracted from the X-ray diffraction patterns (JCPDS standards) [55].

As shown in Fig. 12a, any agglomerate is composed of fine nanoparticles, confirming the high crystallinity degree of the corrosion products of the MHM0 sample. With regards the Fig. 12e, the presence of rings in the SAED pattern of the as-deposited products on the MHM0 sample confirmed the poly-crystalline nature of the corrosion products; however, the sharp bright spots shown may be due to the individual formation of larger particles with specific lattice planes [56]. The rings in the SAED pattern of area 1 in Fig. 12a can be considered to be (002), (210), (211), (310), (222), (213), (004) and (304) reflections of hexagonal HA (Fig. 12e),

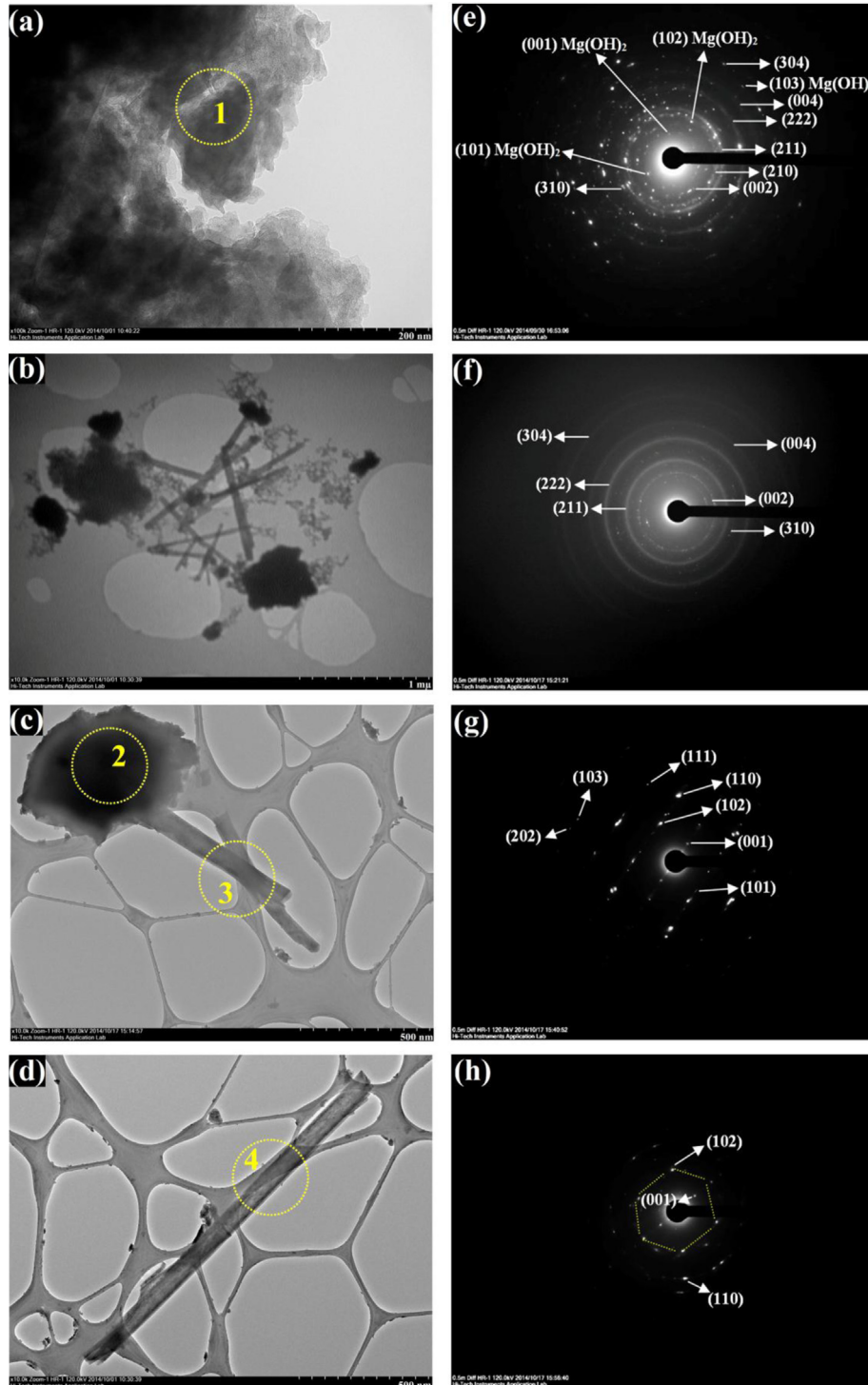


Fig. 12. TEM micrographs of corrosion products of (a) the MHM0, (b, c) MHM10 and (d) MHM15 specimens after 168 h of immersion in a SBF solution at 37 °C. Selected area electron diffraction (SAED) of (e) area 1, (f) area 2, (g) area 3 and (h) area 4.

which agrees with the XRD results. The calculated interplanar spacings of approximately 4.46, 2.37, 1.78 and 1.37 Å, which can correspond to the (001), (101), (102) and (103) planes of $\text{Mg}(\text{OH})_2$, respectively, indicate the presence of $\text{Mg}(\text{OH})_2$ in the corrosion products of the MHM0 sample after 7 days of immersion in the SBF solution. Fig. 12b shows a low-magnification TEM image of the corrosion products, which consist of nanorods and irregularly shaped particles that formed on the surface of the MHM10 sample

after 7 days of immersion in the SBF solution. The SAED pattern in Fig. 12f focused on the irregular agglomerates (area 2 in Fig. 12c) and verified the formation of the hydroxyapatite phase and the decrease in the crystallinity of the agglomerates compared to that in the corrosion products of the MHM0 sample. The decrease in the crystallinity degree of the agglomerates can be showed by the decrease in the number of sharp bright spots in the SAED patterns and to the increase in the width of the rings compared to that of the

rings in the SAED patterns of the corrosion products of the MHM0 sample. The decrease in the crystallinity degree of the agglomerates can be caused by decreasing the amount of HA nanoparticles in the raw material of the Mg/HA/MgO nanocomposites, which act as the nuclei for nucleation of crystalline HA during immersion in the SBF solution. After 7 days of immersion in the SBF solution, the amorphous CaP compounds appeared with the decreasing concentration of HA nanoparticles in the raw material of the MHM samples, indicating that a higher concentration of HA nanoparticles could facilitate the formation of crystalline phases CaP. The SAED of area 3 in Fig. 12c performed on the nanorods in the corrosion products of the MHM10 sample showed a linear array of diffraction spots with a hexagonal crystalline structure that further confirmed the presence of polycrystalline areas at different positions on the rod-like particles (Fig. 12g). The inter-planar distances calculated were 4.46, 2.37, 1.78, 1.56, 1.49, 1.37 and 1.19 Å which agree with the lattice spacing of the Mg(OH)₂ (001), (101), (102), (110), (111), (103) and (202) planes. As shown in Fig. 12d, the rod-like nanoparticles with an average diameter of 60–80 nm and a length of 500–2000 nm are found among the corrosion products of the MHM15 sample after 7 days of immersion in the SBF solution. By focusing the electron beam on a single nanorod in the corrosion products of the MHM15 sample (area 4 in Fig. 12d), the presence of sharp bright spots in the obtained SAED pattern showed the crystalline face of hexagonal Mg(OH)₂, indicating the single-crystalline nature of the nanorods (Fig. 12h). These suggest the relatively high surface nucleation of the MHM15 nanocomposites and the special function of the presence of the MgO nanoparticles in the raw material for the crystallization and the consequent aggregation of the rod-like Mg(OH)₂ crystals [57].

XPS analysis was performed to determine the chemical composition of the corrosion products of MHM samples after 168 h of immersion in the SBF solution (Fig. 13). Each element exhibits the characteristic binding energy in the XPS spectra. The XPS survey scan spectra reveal the presence of Mg, O, Ca, P and C on MHM samples. The binding energy of C 1s peak at ~286 eV confirms the formation of carbonates on the MHM samples in SBF solution as a result of the inadvertent contamination. The binding energies of Ca 2p and P 2p peaks correspond to the calcium phosphate components that deposited on the MHM samples by 7 days of immersion in SBF solution. High-resolution X-ray photoelectron spectra are acquired for Ca 2p, and P 2p peaks (Fig. 14). As shown in Fig. 14, the

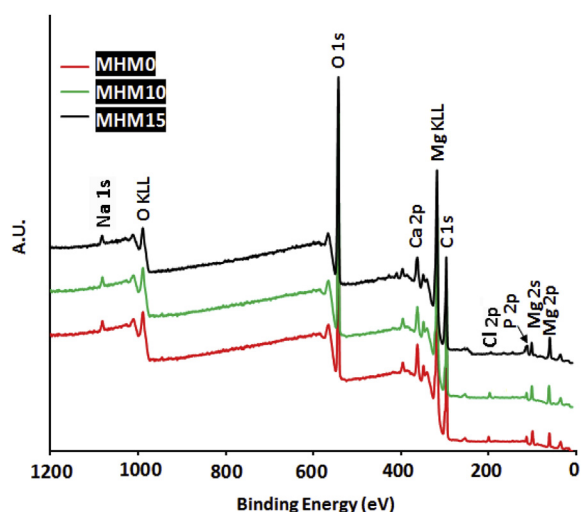


Fig. 13. Survey XPS spectra of the MHM samples after 168 h of immersion in a SBF solution at 37 °C.

binding energy of Ca 2p_{1/2} peaks at ~347.3 eV can be attributed to the presence of HA whereas the binding energy of Ca 2p_{3/2} peak at ~346.7 eV is corresponded to the Ca₃(PO₄)₂ phase [58]. The P 2p spectrum consist of three peaks (Fig. 14) which include the P 2p_{1/2} peak at ~133.2 eV and P 2p_{3/2} peak at ~132.6 eV corresponding to the Ca₃(PO₄)₂ and HA, respectively [59]. Amorphous CaP compounds are formed on the MHM samples during the immersion process, which contributes to the presence of Ca 2p peak at ~345.8 eV (Fig. 14e–h) and P 2p peaks at ~131.3 eV (Fig. 14a–d) [58]. In addition, increases in the intensities of P 2p_{1/2} and Ca 2p_{1/2} spectra were observed in the MHM15 and MHM10 samples compared to those of the MHM0 and MHM5 samples, indicating a larger amount of Ca₃(PO₄)₂ had formed in the corrosion products of the MHM15 and MHM10 samples. However, the intensities of the P 2p_{3/2} and Ca 2p_{3/2} peaks in the MHM15 and MHM10 samples were smaller, indicating that the formation of HA in the corrosion products was restricted by the reduction of HA in the raw material of the MHM samples. In addition, the O 1s signal at a binding energy of ~531 eV can be attributed to the phosphate (PO₄³⁻) groups, the hydroxyl (–OH) groups [60,61] and the carbonate (CO₃²⁻) group. The Mg 2p spectra (Fig. 13) show a single peak at a binding energy (BE) of 50.5 ± 0.1 eV, which corresponds to magnesium hydroxide [62,63]. By increasing the amount of MgO in the raw material of the Mg/HA/MgO nanocomposite, the intensity of the Mg 2p spectra was increased, indicating the presence of larger amounts of Mg(OH)₂ in the corrosion products of the MHM15 and MHM10 samples compared to those of the MHM0 and MHM5 samples. The Cl 2p and Na 1s XPS spectra on the surface of the MHM samples after immersion for 7 days may be associated with the presence of Cl⁻ and Na⁺ ions in the SBF solution [63].

3.2. Physical and mechanical measurements

Table 2 shows that MHM0 sample has the highest ultimate strength compared to other MHM nanocomposites. No significant increase in the ultimate strength was observed when the HA content was reduced from 20 wt% to 5 wt% and the addition of 15 wt% MgO, however, the compressive failure strain significantly increased from 4.4% to 11.8%. By increasing of HA in raw material, the agglomeration of HA particles in the MHM composites restricted the movement of dislocations, thus increasing the difficulty to activate deformation by dislocation motion. It can increase the ultimate strength of MHM samples. The voids/cracks around the HA particles are due to the local increase in volume fraction of HA particles within the agglomerates and give rise to high stress concentration. This accelerates void/crack formation/propagation causing fracture at relatively lower strain. As a result, the agglomeration of HA particles significantly decreased the compressive failure strain of the MHM nanocomposites. The relative density of the MHM0 and MHM5 samples is 0.86 and 0.89 of their theoretical values whereas this value reached to 0.94 and 0.95 in MHM10 and MHM15 samples, respectively. The increased density can be attributed to the increase in compressive ductility of MHM samples by decreasing of HA as well as increasing of Mg and MgO in MHM nanocomposites. The number of voids and pores around the particles within the HA agglomerates decreased by decreasing of HA in raw material that caused the relative density to increase in MHM10 and MHM15 samples under a similar manufacturing process parameters.

Fig. 15 illustrates the polarization corrosion resistance versus the relative density of MHM samples. As can be seen, the corrosion resistance increased by increasing the relative density of nanocomposites, which can be attributed to the penetration of lower amount of corrosive solution within the denser substrates. The pores and voids in sample substrates decreased by increasing of

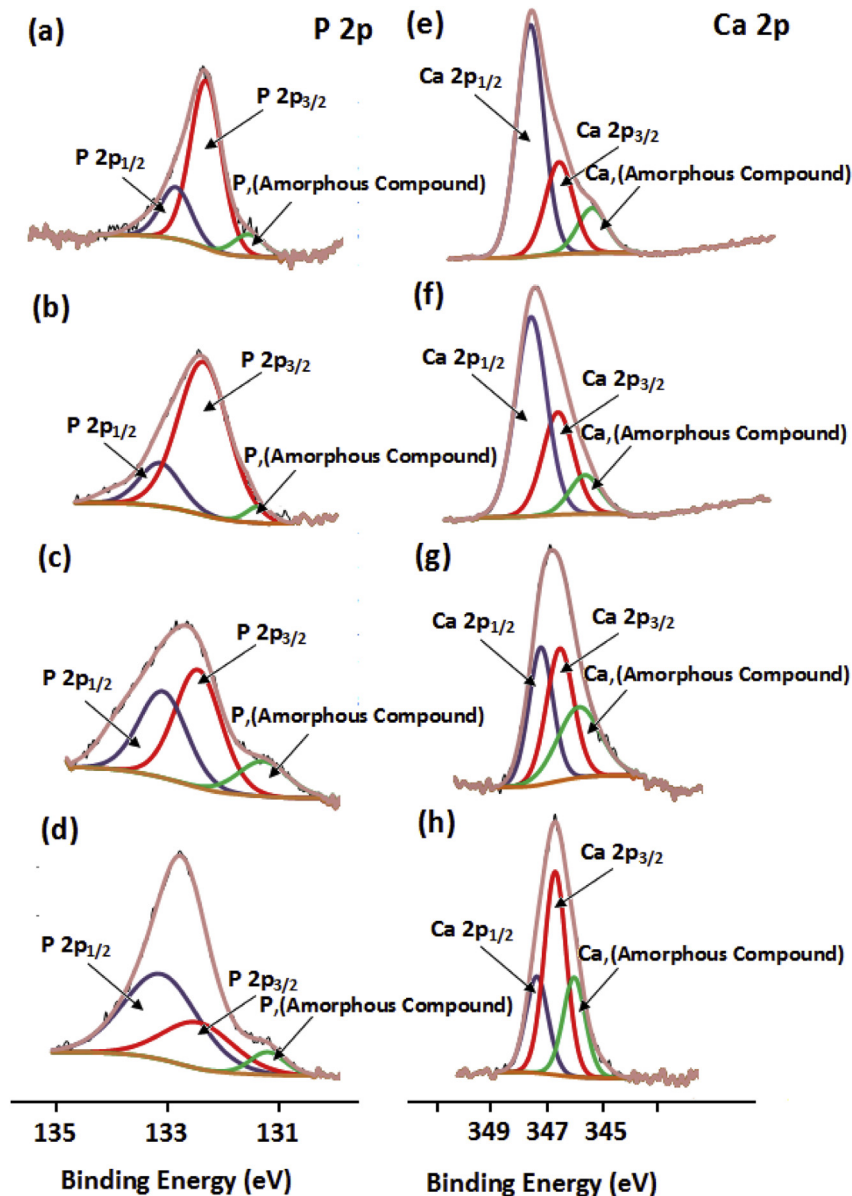


Fig. 14. Detailed XPS spectra of the P2p and Ca2p picks of the (a, e) MHM0, (b, f) MHM5, (c, g) MHM10 and (d, h) MHM15 samples after 168 h of immersion in a SBF solution at 37 °C.

Table 2
Relative, measured and theoretical densities and compression properties of MHM samples.

Sample	MHM0	MHM5	MHM10	MHM15
Relative Density (% theoretical density)	0.86	0.89	0.94	0.95
Measured density	1.830	1.882	1.974	2.002
Theoretical density	2.129	2.115	2.101	2.086
Ultimate Compressive strength-UCS (MPa)	237 ± 6	202 ± 11	198 ± 9	183 ± 14
Compressive failure strain ε (%)	4.2 ± 0.4	4.4 ± 0.6	11.5 ± 2.1	11.8 ± 1.7

relative density that led to the penetration of lower amount of corrosive solution in the sample substrates. This is confirmed by the contact angle measurements as shown in Fig. 4.

3.3. *In vitro* biocompatibility assessments

MTT assays were performed on MHM0, MHM10 and MHM15 samples at 3, 7 and 9 days to evaluate of the viability of normal human osteoblast cells (NHOst). The cell density (proliferation and

differentiation) of osteoblast NHOst cells cultured on the MHM samples were then determined (Fig. 16a). Results showed that the osteoblast cells that proliferated on the MHM nanocomposites displayed a time-dependent behavior. After 3 and 7 days of cell culture, the proliferation and differentiation of cells was less on the MHM0 sample than on the MHM10 samples. This can be attributed to the formation of higher amount of unwanted, possibly harmful hydrogen gas by rapid corrosion and degradation rates in MHM0 sample that might adversely affect the biocompatibility of MHM0

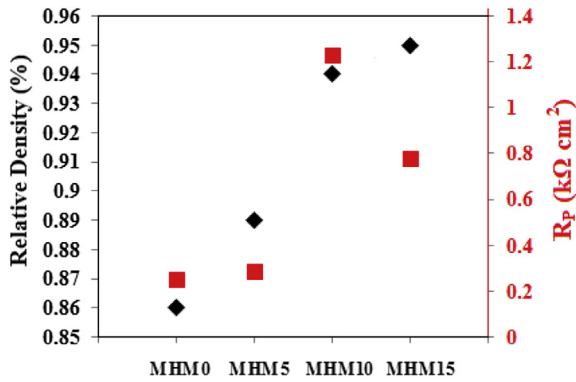


Fig. 15. The polarization corrosion resistance versus the relative density of MHM samples.

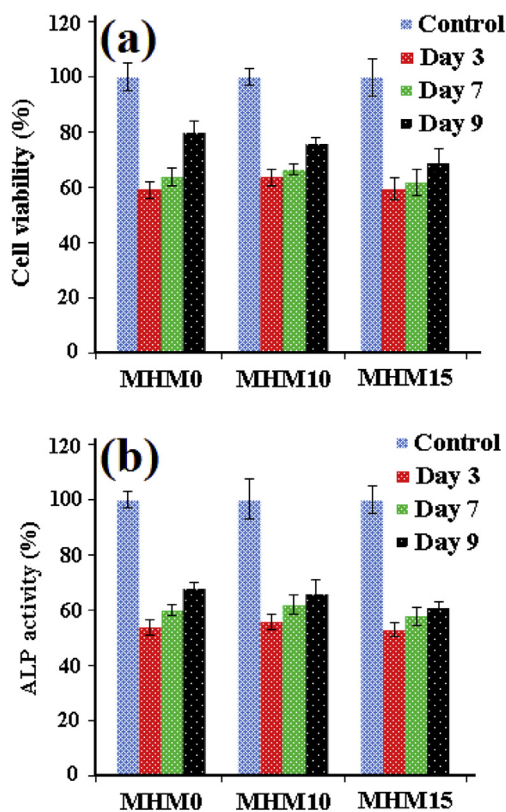


Fig. 16. (a) MTT assay results show normal human osteoblast (NHOst) cells proliferation on MHM0, MHM10 and MHM15 samples after 3, 7 and 9 days of culture, (b) ALP activity tests of MHM0, MHM10 and MHM15 samples after 3, 7 and 9 days of culture. The data are presented as mean \pm SD and values with $P < 0.05$ were considered as statistically non-significant.

sample after 3 and 7 days of cell culture. In addition, the reduction in cell viability of MHM0 sample compared to that of the MHM10 sample may be due to the pH induction caused by rapid degradation of the MHM0 sample in first few days of immersion [64]. However, after 9 days of cell culture, MHM0 sample showed higher level of cell density compared to the MHM10 and MHM15 samples. These results indicate an enhance in the biocompatibility and cell growth of the MHM samples by increasing HA nanoparticles in the raw material, supporting that HA nanoparticles have an important role to provide a suitable environment for living bone cells. However, no significant differences were noticed in the cell viability of the MHM composites indicating good biosafety, as well as

continuous cell growth in these samples by the addition of different amount of MgO and decreasing of HA. Clearly, MTT assay is the most common method being used for evaluating the cytotoxicity of biomaterials. However, further investigations, including ALP activity will be needed to make sure of the biocompatibility of the Mg-based alloys [65–67].

The grown cells were stained to elicit alkaline phosphatase (ALP) enzyme to support the ability of bonelike formation [45]. The differentiation of osteoblast bone cells can be evaluated by ALP activity as a marker of osteoblastic activity. After 3 days of cell culture, ALP results (Fig. 16b) revealed a reduction in ALP activity on the MHM composites than the controlled sample. This decrease in ALP activity is probably due to the surviving behavior of the cells seeded on the different MHM samples and less induced osteogenic phenotype at the beginning of mineralization. A greater increase in ALP activity was observed on MHM0 nanocomposite after 9 days of cell culture, compared to MHM10 and MHM15 samples. This confirms the important role of HA nanoparticles in the stimulation of bone cell response and bone regeneration. Therefore, the presence of more amount of HA nanoparticles in the raw material of MHM samples enhanced the differentiation activity of NHOst cells from day 3–9. A significant enhance was also reported on the ALP activity of human fetal osteoblast (hFOB) cells on membrane scaffolds sprayed with HA nanoparticles compared to as-electrospun blended biocomposite scaffolds [68]. As reported by Chou et al., the presence of more HA in samples might supply higher amount of inorganic free phosphate to stimulate early and high levels of cellular response [69]. Due to the osteoconductivity and osteoinductivity of HA, it has been considered as the ideal material to build bone tissue engineering implants. The fact that HA can absorb more proteins such as fibronectin and vitronectin from the serum promote good binding with integrins, and as a result, osteoconductivity of samples consisting of more HA nanoparticles was improved. With regards to the selective adsorption of adhesive proteins, and the regulation of cellular behaviors such as adhesion, migration, proliferation and differentiation that can result from the specific interaction of the extracellular matrix parameters and their integrin receptors, it is reasonable that the interaction of the adhesive proteins adsorbed to the surface of MHM samples and the integrins on the surface of the osteoblasts contribute to the good cellular responsiveness observed with the MHM nanocomposites consisting HA nanoparticles [67].

4. Conclusion

A blend-cold press-sinter powder metallurgy technique was used for fabrication of the Mg/HA/MgO nanocomposites to use as the biodegradable bone implant materials. According to the contact angle measurements, the penetration of the SBF solution in the substrate of the nanocomposites was intensified by increase of the pores and voids around the local agglomerates of the HA particles, and consequently, the corrosion resistance of the nanocomposites decreased by increasing the HA content in the raw material. The corrosion rate and ultimate compressive strength decreased with the addition of 10 wt% of MgO and the reduction of HA from 27.5 to 12.5 wt%, based on the electrochemical, immersion and compression tests; however, the compressive failure strain (ϵ) increased. The corrosion products that formed on the composite surfaces were primarily composed of $Mg(OH)_2$ nanorods with a hierarchical microstructure, HA, $Ca_3(PO_4)_2$ and amorphous CaP compounds. Based on XRD and SAED analyses, the crystallinity of HA in the corrosion products decreased after reducing the HA content in the raw material. The amount of $Mg(OH)_2$, $Ca_3(PO_4)_2$ and amorphous CaP compounds in the corrosion products decreased after increasing the HA content and decreasing the MgO content in the

raw material of the nanocomposites. The biocompatibility of Mg/HA/MgO nanocomposite for use in new biomaterials was confirmed by the MTT assay and ALP activity.

Acknowledgments

The first author is a recipient of the International Doctoral Fellowship (IDF) scheme from Universiti Teknologi Malaysia. This study was financially sponsored by the FRGS grants from the Ministry of Education Malaysia, eScience Fund grants from the Ministry of Science, Technology and Innovation Malaysia, and UTM Research University grants.

References

- [1] B. Basu, D.S. Katti, A. Kumar, *Advanced Biomaterials: Fundamentals, Processing, and Applications*, John Wiley & Sons, 2010.
- [2] M. Niinomi, *Metall. Mater. Trans. A* 33 (2002) 477–486.
- [3] A. Janković, S. Eraković, M. Mitić, I.Z. Matić, Z.D. Juranić, G.C.P. Tsui, C.Y. Tang, V. Mišković-Stanković, K.Y. Rhee, S.J. Park, *J. Alloy Compd.* 624 (2015) 148–157.
- [4] K. Yu, L. Chen, J. Zhao, S. Li, Y. Dai, Q. Huang, Z. Yu, *Acta Biomater.* 8 (2012) 2845–2855.
- [5] B. Heublein, R. Rohde, V. Kaese, M. Niemeyer, W. Hartung, A. Haverich, *Heart* 89 (2003) 651–656.
- [6] F. Witte, V. Kaese, H. Haferkamp, E. Switzer, A. Meyer-Lindenberg, C.J. Wirth, H. Windhagen, *Biomaterials* 26 (2005) 3557–3563.
- [7] S.S. Nene, B.P. Kashyap, N. Prabhu, Y. Estrin, T. Al-Samman, *J. Alloy Compd.* 615 (2014) 501–506.
- [8] H. Watanabe, Y. Sasakura, N. Ikeo, T. Mukai, *J. Alloy Compd.* 626 (2015) 60–64.
- [9] M.P. Staiger, A.M. Pietak, J. Huadmai, G. Dias, *Biomaterials* 27 (2006) 1728–1734.
- [10] F. Witte, J. Fischer, J. Nellesen, H.-A. Crostack, V. Kaese, A. Pisch, F. Beckmann, H. Windhagen, *Biomaterials* 27 (2006) 1013–1018.
- [11] F. Witte, H. Ulrich, M. Rudert, E. Willbold, *J. Biomed. Mater. Res. Part A* 81 (2007) 748–756.
- [12] F. Witte, H. Ulrich, C. Palm, E. Willbold, *J. Biomed. Mater. Res. Part A* 81 (2007) 757–765.
- [13] Y. Xiong, C. Lu, C. Wang, R. Song, *J. Alloy Compd.* 625 (2015) 258–265.
- [14] B. Homayun, A. Afshar, *J. Alloy Compd.* 607 (2014) 1–10.
- [15] X. Ma, S. Zhu, L. Wang, C. Ji, C. Ren, S. Guan, *J. Alloy Compd.* 590 (2014) 247–253.
- [16] A. Zakyyuddin, K. Lee, *J. Alloy Compd.* 629 (2015) 274–283.
- [17] L.X. Wang, G. Fang, M.A. Leeflang, J. Duszczky, J. Zhou, *J. Alloy Compd.* 622 (2015) 121–129.
- [18] F. Witte, F. Feyereabend, P. Maier, J. Fischer, M. Störmer, C. Blawert, W. Dietzel, N. Hort, *Biomaterials* 28 (2007) 2163–2174.
- [19] X. Gu, W. Zhou, Y. Zheng, L. Dong, Y. Xi, D. Chai, *Mat. Sci. Eng. C* 30 (2010) 827–832.
- [20] K.A. Khalil, A.A. Almajid, *Mater. Des.* 36 (2012) 58–68.
- [21] S.Z. Khalajabadi, M.R. Abdul Kadir, S. Izman, M.Z. Mohd Yusop, *Appl. Surf. Sci.* 324 (2015) 380–392.
- [22] S.Z. Khalajabadi, M.R. Abdul Kadir, S. Izman, M. Kasiri-Asgarani, *Surf. Coat. Technol.* 277 (2015) 30–43.
- [23] X. Wang, L.H. Dong, J.T. Li, X.L. Li, X.L. Ma, Y.F. Zheng, *Mater. Sci. Eng. C* 33 (2013) 4266–4273.
- [24] X.L. Ma, L.H. Dong, X. Wang, *Mater. Des.* 56 (2014) 305–312.
- [25] X. Wang, P. Zhang, L.H. Dong, X.L. Ma, J.T. Li, Y.F. Zheng, *Mater. Des.* 54 (2014) 995–1001.
- [26] S.H. Kwon, Y.K. Jun, S.H. Hong, H.E. Kim, *J. Eur. Ceram. Soc.* 23 (2003) 1039–1045.
- [27] V.K. Mishra, B.N. Bhattacharjee, O. Parkash, D. Kumar, S.B. Rai, *J. Alloy Compd.* 614 (2014) 283–288.
- [28] C.Q. Ning, Y. Zhou, *Biomaterials* 23 (2002) 2909–2915.
- [29] E.S. Thian, N.H. Loh, K.A. Khor, S.B. Tor, *Biomaterials* 23 (2002) 2927–2938.
- [30] A.K. Khanra, H.C. Jung, K.S. Hong, K.S. Shin, *Mater. Sci. Eng. A* 527 (2010) 6283–6288.
- [31] P. Amaravathy, S. Sathyanarayanan, S. Sowndarya, N. Rajendran, *Ceram. Int.* 40 (2014) 6617–6630.
- [32] L. Mohan, D. Durgalakshmi, M. Geetha, T.S.N. Sankara Narayanan, R. Asokamani, *Ceram. Int.* 38 (2012) 3435–3443.
- [33] A.K. Gain, L. Zhang, W. Liu, *Mater. Des.* 67 (2015) 136–144.
- [34] A. Farzin, M. Ahmadian, M. Fathi, *Mater. Sci. Eng. C* 33 (2013) 2251–2257.
- [35] D. Pereira, S. Cachinho, M. Ferro, M. Fernandes, *J. Eur. Ceram. Soc.* 24 (2004) 3693–3701.
- [36] R. Richards, W. Li, S. Decker, C. Davidson, O. Koper, V. Zaikovski, A. Volodin, T. Rieker, K.J. Klabunde, *J. Am. Chem. Soc.* 122 (2000) 4921–4925.
- [37] C. Goh, M. Gupta, J. Wei, L. Lee, *J. Compos. Mater.* 41 (2007) 2325–2335.
- [38] T. Lei, W. Tang, S.H. Cai, F.F. Feng, N.F. Li, *Corros. Sci.* 54 (2012) 270–277.
- [39] S.Z. Khalajabadi, M.R. Abdul Kadir, S. Izman, H.R. Bakhsheshi-Rad, S. Farahany, *Ceram. Int.* 40 (2014) 16743–16759.
- [40] S.Z. Khalajabadi, M.R. Abdul Kadir, S. Izman, A. Samavati, Z. Othaman, *Ceram. Int.* 41 (2015) 11346–11358.
- [41] B. Nasiri-Tabrizi, A. Fahami, R. Ebrahimi-Kahrizangi, *Ceram. Int.* 39 (2013) 5751–5763.
- [42] T. Kokubo, H. Takadama, *Biomaterials* 27 (2006) 2907–2915.
- [43] A. Sudholz, K. Gusieva, X. Chen, B. Muddle, M. Gibson, N. Birbilis, *Corros. Sci.* 53 (2011) 2277–2282.
- [44] N.J. Hallab, C. Vermes, C. Messina, K.A. Roebuck, T.T. Glant, J.J. Jacobs, *J. Biomed. Res. A* 60 (2002) 420.
- [45] Y. Zhang, V.J. Reddy, S.Y. Wong, X. Li, B. Su, S. Ramakrishna, C.T. Lim, *Tissue Eng. Part A* 16 (2010) 1949–1960.
- [46] M. Razavi, M. Fathi, M. Meratian, *Mater. Sci. Eng. A* 527 (2010) 6938–6944.
- [47] M. Ren, S. Cai, T. Liu, K. Huang, X. Wang, H. Zhao, S. Niu, R. Zhang, X. Wu, *J. Alloy Compd.* 591 (2014) 34–40.
- [48] H. Bakhsheshi-Rad, M. Abdul-Kadir, M. Idris, S. Farahany, *Corros. Sci.* 64 (2012) 184–197.
- [49] Z. Shi, M. Liu, A. Atrens, *Corros. Sci.* 52 (2010) 579–588.
- [50] M. Bormapour, M. Celikin, M. Cerruti, M. Pekguleryuz, *Mater. Sci. Eng. C* 35 (2014) 267–282.
- [51] Y. Lu, A.R. Bradshaw, Y.L. Chiu, I.P. Jones, *J. Alloy Compd.* 614 (2014) 345–352.
- [52] M. Ascencio, M. Pekguleryuz, S. Omanovic, *Corros. Sci.* 87 (2014) 489–503.
- [53] H.R. Bakhsheshi-Rad, M.H. Idris, M.R. Abdul-Kadir, A. Ourdjini, M. Medraj, M. Daroonparvar, E. Hamzah, *Mater. Des.* 53 (2014) 283–292.
- [54] A. Srinivasan, P. Ranjani, N. Rajendran, *Electrochim Acta* 88 (2013) 310–321.
- [55] M.R. Varma, C. Reshmi, P.N. Lekshmi, INTECH Open Access Publisher, 2011.
- [56] M.K. Suresh, J.K. Thomas, H. Sreemoolanadhan, C.N. George, A. John, S. Solomon, P.R.S. Warier, J. Koshy, *Mater. Res. Bull.* 45 (2010) 761–765.
- [57] Y. Gao, H. Wang, Y. Su, Q. Shen, D. Wang, *J. Cryst. Growth* 310 (2008) 3771–3778.
- [58] Y. Pan, S. He, D. Wang, D. Huang, T. Zheng, S. Wang, P. Dong, C. Chen, *Mater. Sci. Eng. C* 47 (2015) 85–96.
- [59] J. Zhang, N. Kong, Y. Shi, J. Niu, L. Mao, H. Li, M. Xiong, G. Yuan, *Corros. Sci.* 85 (2014) 477–481.
- [60] H. Wang, S. Zhu, L. Wang, Y. Feng, X. Ma, S. Guan, *Appl. Surf. Sci.* 307 (2014) 92–100.
- [61] Z.Q. Yao, Y. Ivanisenko, T. Diemant, A. Caron, A. Chuvilin, J.Z. Jiang, R.Z. Valiev, M. Qi, H.J. Fecht, *Acta Biomater.* 6 (2010) 2816–2825.
- [62] H. Li, S. Pang, Y. Liu, L. Sun, P.K. Liaw, T. Zhang, *Mater. Des.* 67 (2015) 9–19.
- [63] A.A. El-Hadad, V. Barranco, A. Samaniego, I. Llorente, F.R. García-Galván, A. Jiménez-Morales, J.C. Galván, S. Feliu Jr., *Prog. Org. Coat.* 77 (2014) 1642–1652.
- [64] X.N. Gu, N. Li, Y.F. Zheng, L. Ruan, *Mater. Sci. Eng. B* 176 (2011) 1778–1784.
- [65] X. Qiu, P. Wan, L.L. Tan, X.M. Fan, K. Yang, *Mater. Sci. Eng. C* 36 (2014) 65–76.
- [66] T. Zhang, X. Wu, H. Huang, Y. Zhang, M. Li, G. Lan, H. Xia, Q. Yin, *Mater. Lett.* 137 (2014) 362–365.
- [67] A. Abdal-hay, P. Vanegas, A.S. Hamdy, F.B. Engel, J.H. Lim, *Chem. Eng. J.* 254 (2014) 612–622.
- [68] D. Gupta, J. Venugopal, S. Mitra, V.R. Giri, S. Dev Ramakrishna, *Biomaterials* 30 (2009) 2085–2094.
- [69] R. Rai, M. Tallawi, N. Barbani, C. Frati, D. Madeddu, S. Cavalli, G. Graiani, F. Quaini, J.A. Roether, D.W. Schubert, E. Rosellini, A.R. Boccaccini, *Mater. Sci. Eng. C* 33 (2013) 3677–3687.